Supplementary Note 1 – Comparison of integrated approach and non-integrated approaches

We compared our integrated solar electrolysis approach "Concentrated PV + SOE stack" to "Standard PV + SOE stack" and "Standard PV + PEM stack". As a reference we used the simulated reference case. From the STH efficiency, $\eta_{STH} = \dfrac{\Delta \dot{n}_{H_2} \cdot HHV_{H_2}}{\dot{Q}_{solar,PV} + \dot{Q}_{solar,th}}$, we derived a system level STH efficiency defined $\eta_{STH,system} = \dfrac{\eta_{stack} \cdot P_{stack}}{\dot{Q}_{abs} \cdot {1}\big/{\eta_{STT} \cdot \eta_{optical,th}} + P_{stack} \cdot {1}\big/{\eta_{PV} \cdot \eta_{PV} \cdot \eta_{optical,PV}}}$. We assumed that P_{stack}, $\dot{Q}_{abs}$, and η_{STT} are constant regardless of the used solar electrolysis approach (except for the case "PV+PEM" where no heat is required, thus $\dot{Q}_{abs} = 0$). From the Sankey diagram (Figure 2) we know $P_{stack} = 41.9$ W, $\dot{Q}_{abs} = 24.5$ W, and $\eta_{STT} = 62.3\%$. The assumed parameters and calculated STH efficiencies for the three solar electrolysis approaches are shown in the Table S1.

Table S1. Comparison table

	η_{stack}	$\eta_{optical,th}$	$\eta_{optical,PV}$	η_{PV}	η_{STH}
CPV+SOE	1.25[a]	0.85[b]	0.85[b]	0.2[c]	0.169
PV+SOE	1.25[a]	0.85[d]	0.70[e]	0.15[f]	0.110
PV+PEM	0.70[g]	–[h]	0.70[e]	0.15[f]	0.068

[a] from reference case (Sankey diagram), i.e. $\eta_{stack} = \Delta \dot{n}_{H_2} \cdot HHV_{H_2} / P_{stack}$

[b] The concentration system is the same for solar thermal and electrical radiation. We assumed a solar dish as concentrator with $\eta_{optical,th} = \eta_{optical,PV} = 0.85$.

[c] The efficiency of the concentrated PV cells was assumed 20%.

[d] As concentrator a solar dish with $\eta_{optical,th} = 0.85$ was assumed.[1]

[e] We assumed tilted PV panels (no tracking) and assumed an annual optical efficiency due to the cosine loss of the sun (normal of the panel not equal to normal of solar irradiation) to 70%.[2]

[f] The efficiency of un-concentrated PV cells was assumed 15%

[g] The electricity-to-hydrogen efficiency of a PEM can be assumed 70%.[3]

[h] For PEM electrolysis no heat is required, thus $\dot{Q}_{abs} = 0$.

The comparison shows that the potential of high-temperature electrolysis using concentrated PV cells is the highest (16.9%), followed by high-temperature electrolysis using electricity from standard PV cells (11%). The lowest potential shows the use of PEM electrolysis and standard PV cells (6.8%). Here, we only compared the approaches in terms of STH efficiency. Other criteria, such as costs or the weighing of the use of rare/abundant materials (catalysts) would have also to be taken into account in a more practical, comparative analysis.

Supplementary Note 2 – Heat transfer model of reactor, discussion of heat losses and heat recovery in the reactor

The flows of the reactant and product enthalpies are shown in Figure S1. The reactants at the inlet before the heat exchanger, $H_{amb} = \sum_i \dot{n}_{i,react} \cdot h_{i,react}(T_{amb})$, are pre-heated to

$H_{pre\text{-}heated} = \sum_i \dot{n}_{i,react} \cdot h_{i,react}(T_{pre\text{-}heated})$, where $\dot{Q}_{HEX} = H_{pre\text{-}heated} - H_{amb}$ is the heat received from the heat exchanger. The pre-heated reactants enter then the solar cavity-receiver and are heated to $H_{cav} = \sum_i \dot{n}_{i,react} \cdot h_{i,react}(T_{cav})$, where $\dot{Q}_{abs,cav} = H_{cav} - H_{pre\text{-}heated}$. After the transmission losses ($\dot{Q}_{trasmission}$) and the heat flux of the SOE stack ($\dot{Q}_{stack}$, see eq. (3), note that the heat flux of the SOE stack can be smaller, equal or larger than 0 indicated by the double arrow), the enthalpy stream leaving the SOE stack is given by $H_{stack} = H_{cav} - \dot{Q}_{stack} - \dot{Q}_{transmission} = \sum_i \dot{n}_{i,prod} \cdot h_{i,prod}(T_{stack})$. Due to further heat losses in the pipes ($\dot{Q}_{exhaust} = H_{stack} - H_{exhaust}$), the enthalpy is reduced to $H_{exhaust} = \sum_i \dot{n}_{i,prod} \cdot h_{i,prod}(T_{exhaust})$ before entering the heat exchanger, where $H_{exhaust} - H_{cooled\text{-}donw} = \dot{Q}_{HEX}$. However, in the presented work we considered $\dot{Q}_{exhaust} = 0$, and thus $T_{stack} = T_{exhaust}$. Finally, the cooled-down product stream, $H_{cooled\text{-}down} = \sum_i \dot{n}_{i,prod} \cdot h_{i,prod}(T_{cooled\text{-}down})$, leaves the system.
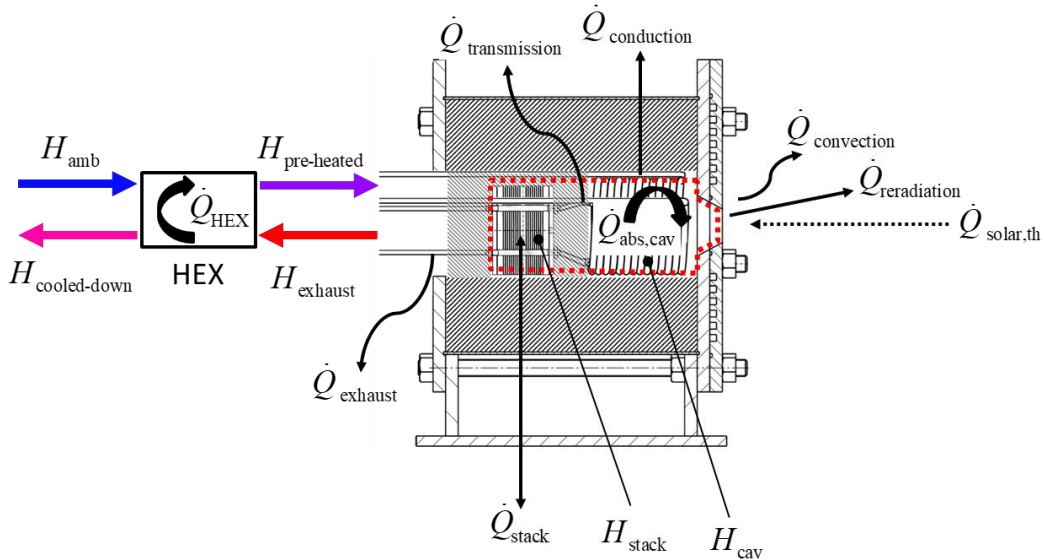

Figure S1. Heat and enthalpy flows of the integrated reactor
Schematic of the reactor showing the enthalpy and heat flows. The heat exchanger is depicted by a rectangular box (HEX). The dotted red line indicates the control volume of the solar cavity-receiver and SOE stack used in the model.

The total thermal input to the reactor is given $\dot{Q}_{\text{thermal}} = \dot{Q}_{\text{HEX}} + \dot{Q}_{\text{solar,th}}$ and the (total) absorbed heat is given $\dot{Q}_{\text{abs}} = \dot{Q}_{\text{abs,cav}} + \dot{Q}_{\text{HEX}}$. The energy conservation at steady-state in the solar cavity-receiver is given $\dot{Q}_{\text{solar,th}} = \dot{Q}_{\text{abs,cav}} + \dot{Q}_{\text{reradiation}} + \dot{Q}_{\text{convection}} + \dot{Q}_{\text{conduction}}$, where the reradiation losses are defined in eq. (1). The convective heat losses out of the cavity are $\dot{Q}_{\text{convection}} = h_{\text{cav}} \cdot A_{\text{aper}} \cdot (T_{\text{cav}} - T_{\text{amb}})$ where h_{cav} is the convective heat transfer coefficient for the solar cavity-receiver. The conductive heat

losses are determined $\dot{Q}_{\text{conduction}} = (T_{\text{cav}} - T_{\text{amb}}) \cdot k \cdot \left[\overbrace{\frac{2\pi L}{\ln(r_2/r_1)}}^{\text{mantel}} + \overbrace{\frac{A_{\text{front}}}{\Delta d}}^{\text{front}} \right]$ where k is the heat

conductivity of the insulation, L the length of the solar cavity-receiver, r_1 and r_2 the inner (cylinder wall of cavity) and outer radius (considering the thickness of the insulation, thus $d = r_2 - r_1$) of the cavity, respectively, and $A_{\text{front}} = \pi r_2^2 - A_{\text{aper}}$.

Heat losses – The energy conservation at steady-state for the solar cavity-receiver of the lumped parameter model is given in eq. (1). The heat losses were modeled explicitly as $\dot{Q}_{\text{loss}} = \dot{Q}_{\text{conduction}} + \dot{Q}_{\text{convection}}$ (i.e. $f_{\text{loss}} = \dot{Q}_{\text{loss}} / \dot{Q}_{\text{thermal}}$). We assumed the geometrical parameters of the solar cavity-receiver (r_1, r_2, d, L) relative to the aperture diameter, D_{aper}, such that $f_{r_1} = r_1 / D_{\text{aper}}$, $f_d = d / D_{\text{aper}}$, and $f_L = L / D_{\text{aper}}$. We investigated the influence of various insulation thicknesses and cavity sizes on the heat loss factor. The baseline parameters are shown in Table S2.
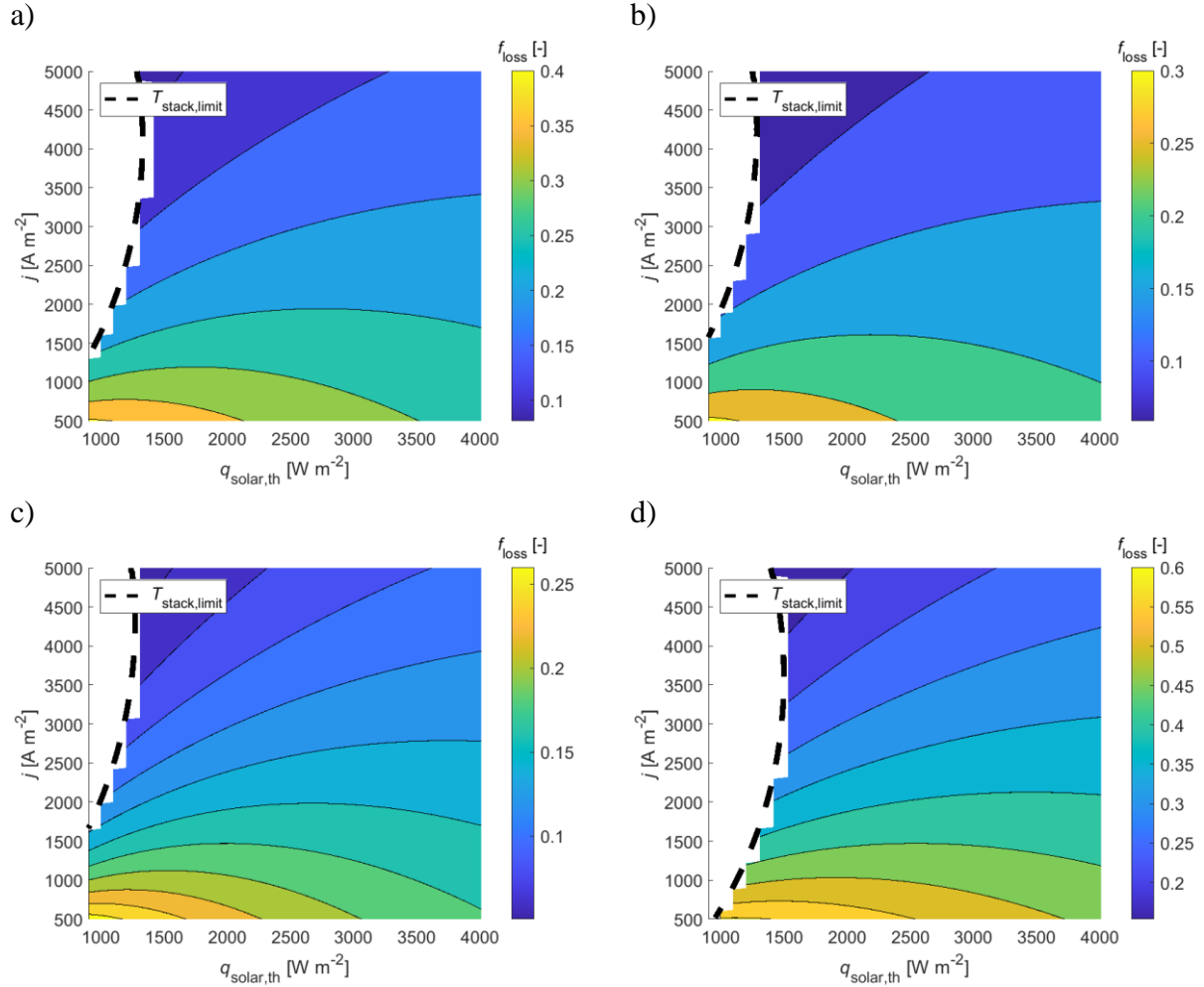
The heat loss factor, f_{loss}, as a function of the solar thermal input and current density is shown in Figure S2 for the cases a) $f_d = 1$, $f_{r1} = 2$, $f_L = 4$, b) $f_d = 2$, $f_{r1} = 2$, $f_L = 4$, c) $f_d = 4$, $f_{r1} = 2$, $f_L = 4$, and d) $f_d = 2$, $f_{r1} = 4$, $f_L = 8$. The heat losses, and thus the heat loss factor, increase with decreasing insulation thickness for a constant cavity size (see case a) to c)). However, doubling the size of the cavity for constant insulation thickness also doubles the heat losses (case b) vs. d)). As an example case, $f_{\text{loss}} = 16.42\%$ for $q_{\text{solar,th}} = 2475$ W m^{-2} and $j = 2500$ A m^{-2} for case b), i.e. with a solar cavity-receiver geometry of $A_{\text{aper}} = 2.1$ cm, $r_1 = 4.2$ cm, $d = 4.2$ cm, and $L = 8.4$ cm. The results show that the heat loss factor ranges typically between 10 – 30%.

Table S2. Baseline parameters for heat loss assessment in solar cavity-receiver
The baseline parameters used for the heat loss assessment in solar cavity-receiver in Supplementary Note 2.

Parameter	Symbol	Unit	Value	Reference
Thermal conductivity	k	W m^{-1} K^{-1}	0.02	assumed
Convective heat transfer coefficient	h_{cav}	W m^{-2} K^{-1}	10	assumed
Ratio insulation thickness to aperture diameter	f_d	-	1, 2, 4	Exp. Setup[a]
Ratio inner radius to aperture diameter	f_{r_i}	-	2, 4	Exp. Setup[a]
Ratio cavity length to aperture diameter	f_L	-	4, 8	Exp. Setup[a]

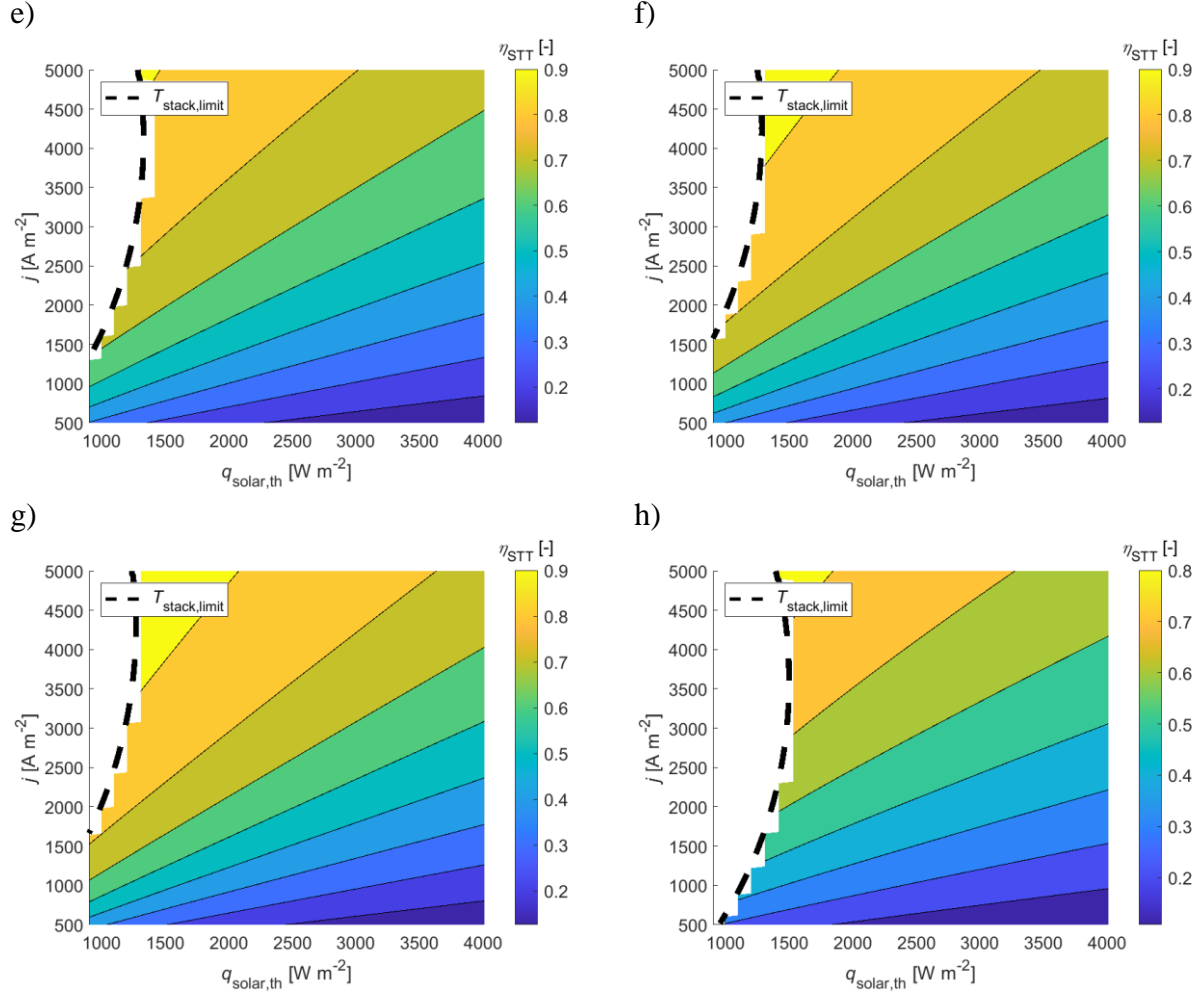[a] Based on geometry of experimental setup

Figure S2. Heat loss factor and STT efficiency assessment for the solar cavity-receiver
Heat loss factor (a to d) and STT efficiency (e to h) of solar cavity-receiver as a function of solar thermal input and current density for a), e) $f_d = 1, f_{r1} = 2, f_L = 4$, b), f) $f_d = 2, f_{r1} = 2, f_L = 4$, c), g) $f_d = 4, f_{r1} = 2, f_L = 4$, and d), h) $f_d = 2, f_{r1} = 4, f_L = 8$. Concentration was constant at $\tilde{C} = 500$, no heat recovery, black dashed lines indicate lower (900 K) and upper (1300 K) stack temperature limit, solar thermal input range is 39 – 173 W, and solar PV input range is 132 – 1842 W.

The STH efficiency as a function of the solar thermal input and current density is shown in Figure S3 for the two extreme cases (resulting in the lowest and highest f_{loss}), i.e. for a) $f_d = 4, f_{r1} = 2, f_L = 4$, and b) $f_d = 2, f_{r1} = 4, f_L = 8$. Both cases show similar maximum STH efficiencies (18-19%) and a large operation range (yellow isosurface) with high STH efficiency with all operation modes (endothermal, thermoneutral and exothermal).
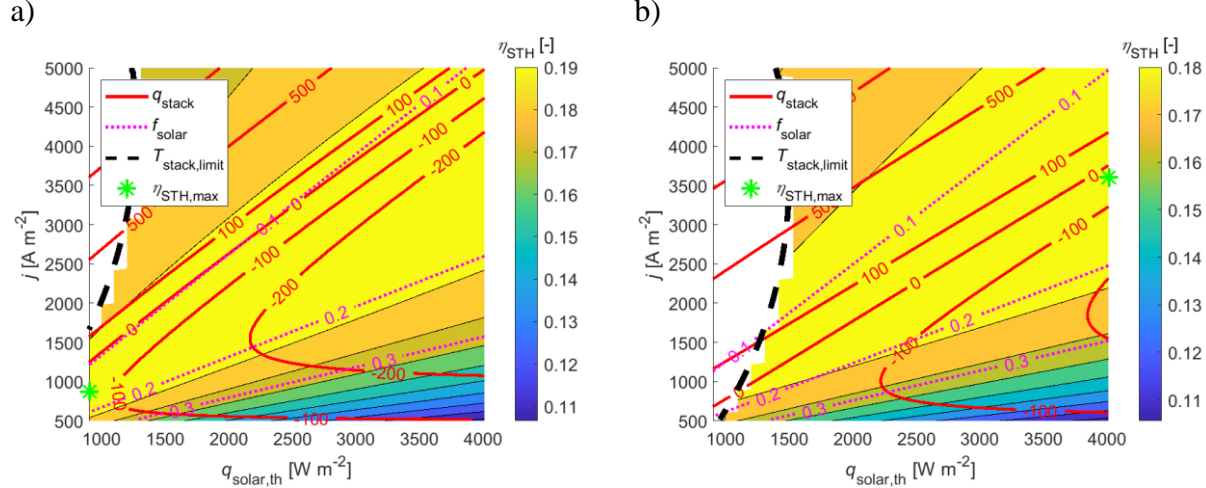
5

Figure S3. STH efficiency analysis of solar reactor for lowest and highest heat loss cases
STH efficiency as a function of solar thermal input and current density for a) $f_d = 4$, $f_{r1} = 2$, $f_L = 4$, and b) $f_d = 2$, $f_{r1} = 4$, $f_L = 8$. Concentration was constant at $\tilde{C} = 500$, no heat recovery, black dashed lines indicate lower (900 K) and upper (1300 K) stack temperature limit, solar thermal input range is 39 – 173 W, and solar PV input range is 132 – 1842 W.

Consequently, we simplified the modeling of the heat losses by assuming $\dot{Q}_{loss} = f_{loss} \cdot \dot{Q}_{thermal}$, where f_{loss} is a constant heat loss factor. The justification for this approach is *i*) the heat losses were within a relatively small range (10 – 30%), and *ii*) the behavior of the STH efficiency (operation modes of the SOE stack) as a function of the solar thermal input and current density is similar to the one observed for the reference case with $f_{loss} = 20\%$ (see Figure 1b).

Heat recovery –Heat recovery is a valuable option for reducing the solar thermal input. However, heat can only be recovered from the exhaust gas streams (see heat exchanger schematic in Figure S1). Other possibilities, such as heat recovery from the solar cavity-receiver (recovering re-radiation or heat losses) are technically not feasible, and thus not considered. The state-of-the-art definition of the heat recovery efficiency or heat exchanger efficiency is $\eta_{HEX} = \dfrac{\dot{Q}_{HEX}}{\Delta H_{stack}}$, describing the amount of heat form the exhaust gas stream that is recovered. For an ideal heat exchanger, $\eta_{HEX} = 1$. In contrast, we defined a heat recovery effectiveness ($\dot{Q}_{thermal} = \dot{Q}_{solar,th} \cdot (1 - \eta_{HR})$), which describes the ratio of heat recovered with regards to the solar thermal input. As an example, the case with $\eta_{HR} = 30\%$ corresponds to $\eta_{HEX} = 84.75\%$. The latter value represents a typical heat exchanger efficiency.

Supplementary Note 3 – Detailed table for experimental campaigns

Table S3 summarizes detailed conditions and results of all experimental runs.

Table S3: Run table for experimental runs

Experimental campaigns with input parameters (input power and flow conditions) and measured output parameters (heat flow, temperature, STT efficiency and STH efficiency, produced H_2 and O_2) for both campaign 1 (type 1 = without SOE stack, type 2 = with

type 1	type 2	$\dot{Q}_{solar,th}$	$\dot{Q}_{solar,PV}$	$Q_{solar,total}$	f_{solar}	SFC (anode/cathode)	N_2 (anode)	Air (anode)	H_2O, liquid (cathode)	H_2 (cathode)	$\dot{Q}_{abs}$	$\dot{Q}_{erad}$	$\dot{Q}_{loss}$	T_{cav}	T_{stack}	j_{TN}	H_2 (cathode)	O_2 (anode)	η_{STT}	η_{STH}
		[W]	[W]	[W]	[%]	[Nml min^{-1} cm^{-2}]	[Nml min^{-1}]	[Nml min^{-1}]	[g min^{-1}]	[Nml min^{-1}]	[W]	[W]	[W]	[K]	[K]	[A m^{-2}]	[Nml min^{-1}]	[Nml min^{-1}]	[%]	[%]
Yes	No	910	-	-	-	-	180	-	2.25	-	143	64	700	975	-	-	-	-	16.03%	-
Yes	No	910	-	-	-	-	360	-	4.50	-	285	63	556	971	-	-	-	-	31.98%	-
Yes	No	910	-	-	-	-	540	-	6.75	-	403	40	462	864	-	-	-	-	44.87%	-
Yes	No	910	-	-	-	-	710	-	9.00	-	526	34	343	832	-	-	-	-	58.59%	-
Yes	No	910	-	-	-	-	860	-	10.80	-	612	28	260	789	-	-	-	-	68.41%	-
Yes	No	910	-	-	-	-	1000	-	12.60	-	670	20	194	725	-	-	-	-	76.53%	-
No	Yes	1468	-	-	-	4/4	-	1728	1.56	172.8	123	55	1290	938	-	-	-	-	8.35%	-
No	Yes	1704	-	-	-	4/4	-	1728	1.56	172.8	129	79	1493	1026	-	-	-	-	7.72%	-
No	Yes	1876	-	-	-	4/4	-	1728	1.56	172.8	132	87	1656	1050	-	-	-	-	7.14%	-
No	Yes	2049	-	-	-	4/4	-	1728	1.56	172.8	137	106	1803	1104	-	-	-	-	6.82%	-
No	Yes	996	-	-	-	8/8	-	3456	3.11	345.6	215	18	776	714	-	-	-	-	20.19%	-
No	Yes	1232	-	-	-	8/8	-	3456	3.11	345.6	230	29	985	798	-	-	-	-	17.64%	-
No	Yes	1468	-	-	-	8/8	-	3456	3.11	345.6	244	42	1193	877	-	-	-	-	15.87%	-
No	Yes	1704	-	-	-	8/8	-	3456	3.11	345.6	253	63	1390	969	-	-	-	-	14.75%	-
No	Yes	2049	-	-	-	8/8	-	3456	3.11	345.6	270	91	1687	1062	-	-	-	-	13.21%	-
-	-	1640	86	1726	95%	2/2	-	864	0.78	86.4	65	73	1502	1007	878	284	94	47	3.95%	1.06%
-	-	1770	124	1894	93%	2/2	-	864	0.78	86.4	67	85	1618	1046	941	411	136	68	3.77%	1.39%
-	-	2050	220	2270	90%	2/2	-	864	0.78	86.4	71	113	1866	1122	1003	811	268	134	3.46%	2.06%
-	-	1640	132	1772	93%	4/4	-	1728	1.56	172.8	128	68	1445	987	856	435	144	72	7.78%	1.58%
-	-	1770	263	2033	87%	4/4	-	1728	1.56	172.8	132	79	1559	1026	923	870	288	144	7.43%	2.74%
-	-	2050	382	2432	84%	4/4	-	1728	1.56	172.8	140	106	1805	1104	967	1265	419	209	6.81%	3.33%

Supplementary Note 4 – Further results of lumped parameter reactor model
For the reference case, the STT efficiency of the solar cavity-receiver is shown in Figure S4. The STT efficiency depends on both, the solar thermal input and the current density. The latter dependency results from the constant overstochiometry ($f_{\text{stoch}} = 2$), i.e. the mass flow rate of the reactants is increasing linearly with increasing current density. The highest $\eta_{\text{STT}} = 79.6\%$ was found for $q_{\text{solar,th}} = 1536$ W m^{-2} and $j = 5000$ A m^{-2}. We observed that the STT efficiency increases monotonically with increasing current density but decreases with increasing solar thermal input. The former is attributed to the increasing mass flow rate, which lowers the solar cavity-receiver temperatures, and thus reduces the reradiation and heat losses. Conversely, increasing the solar thermal inputs results in higher solar cavity-receiver temperatures, and thus increasing the reradiation and heat losses with respect to the absorbed heat.
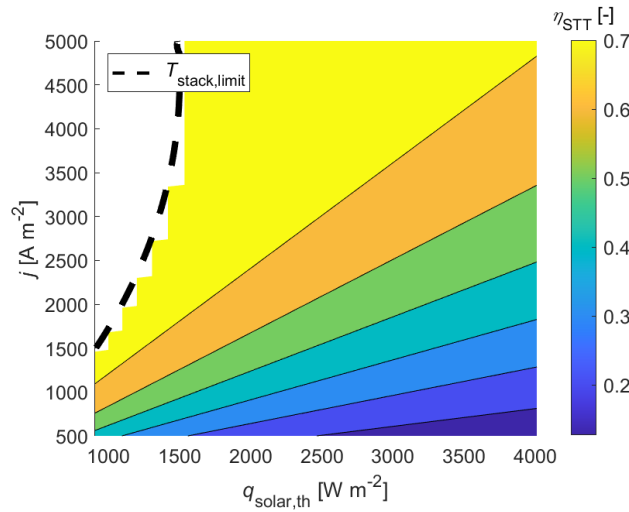

Figure S4. STT efficiency analysis of simulated reference case
STT efficiency (contour plot) as a function of solar thermal input and current density for the reference case. Black dashed lines indicate lower (900 K) stack temperature limit. Concentration was constant at $\tilde{C} = 500$. Solar thermal input range is 39 – 173 W. Solar PV input range is 132 – 1842 W.

The influence of the heat loss factor on the STH efficiency was also studied. Figure S5 shows the STH efficiency as a function of the solar thermal input and current density for a) $f_{\text{loss}} = 10\%$ and b) $f_{\text{loss}} = 30\%$. The other parameters were the same as defined for the reference case. We observed that increasing the heat loss factor decreases the STH efficiencies. However, the differences are marginal (within 1%). Compared to the reference case, we found the same behavior of the STH efficiency (similar maximum STH efficiency, large operation range with all operation modes).
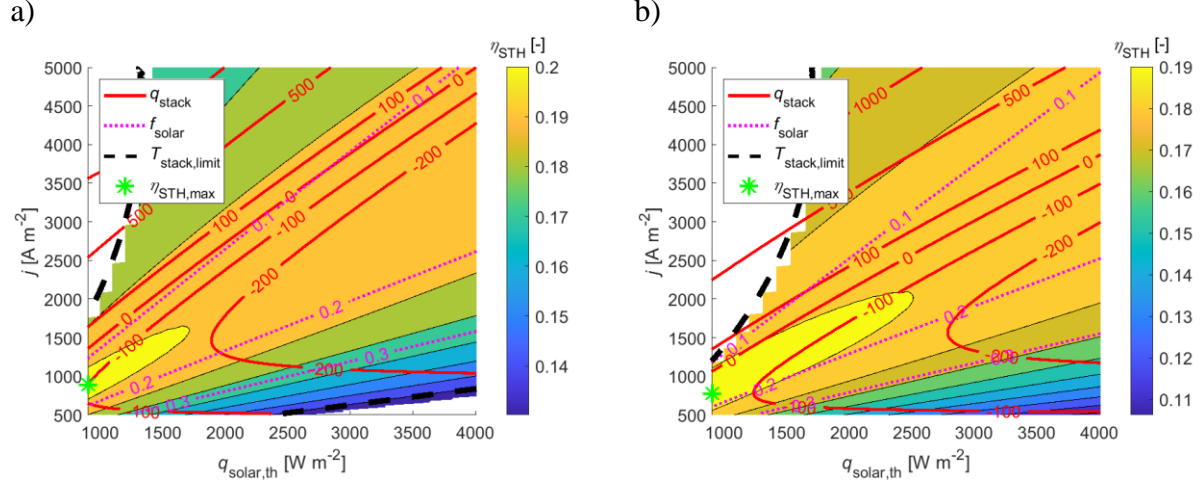
a)   b)

Figure S5. STH efficiency analysis for simulated case with 10% and 30% heat loss factor
STH efficiency (contour plot), heat flux of SOE stack (red solid isolines), and solar power input fraction (magenta dotted isolines) as a function of solar thermal input and current density for a) f_{loss} = 10% and b) f_{loss} = 30%. Black dashed lines indicate lower (900 K) and upper (1300 K) stack temperature limits.

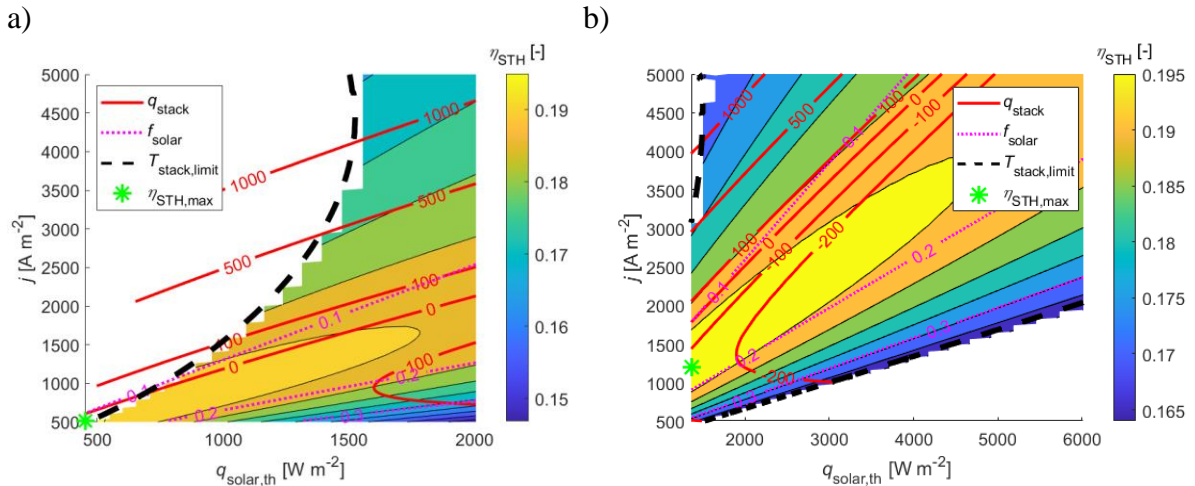a)   b)

Figure S6. STH efficiency analysis of simulated case with solar concentration of 250 and 750
STH efficiency (contour plot), heat flux of SOE stack (red solid isolines), and solar power input fraction (magenta dotted isolines) as a function of solar thermal input and current density for reference case. Black dashed lines indicate lower (900 K) and upper (1300 K) stack temperature limits. Constant concentration was a) $\tilde{C}$ = 250 and b) $\tilde{C}$ = 750. Maximum STH efficiency was for a) 19.53% and b) 19.98% (indicated by green asterisk).

In comparison to the reference case, we investigated the influence of varying the solar concentration at the aperture. The STH efficiency as a function the solar thermal input and the current density using solar concentrations of 250 and 750 is shown in Figure S6. The maximum STH efficiency is for all cases (reference case with $\tilde{C}$ = 250 – 750) within 19.53 – 19.98%, and thus only increased marginally for increasing solar concentration. Considering the best operation

9

ranges (yellow and/or orange area in contour plots), we observed the tendency of favoring more the endothermic SOE stack operation with increasing solar concentration.

The main advantage of increasing the solar concentration is less in increasing the STH efficiency but reducing the aperture size for the solar cavity-receiver and the required area for the PV cells. However, the requirements for the solar concentrator are higher in order to achieve higher solar concentrations. Furthermore, the higher solar concentration induces more thermal stress in the solar cavity-receiver ("hot spots") and requires more sophisticated PV cells together with thermal management.

We investigated the effect of the heat recovery effectiveness. The STH efficiency as a function the solar thermal input and the current density with heat recovery effectiveness of 10% ($\eta_{HX} = 28.8\%$) and 20% ($\eta_{HX} = 59.3\%$) in Figure S7. In comparison to the reference case and the case with $\eta_{HR} = 30\%$, we observed maximum STH efficiencies $\eta_{STH} = 19.85\%$, 20.15%, 20.48% and 20.83% for $\eta_{HR} = 0\%$, 10%, 20% and 30%, respectively. As expected, the increase of the heat recovery effectiveness increases the STH efficiency. We observed that the operation range for high STH efficiencies (range from maximum to 1% below maximum) is shifted towards higher endothermic SOE operation ($q_{stack} < 0$) for increasing heat recovery.
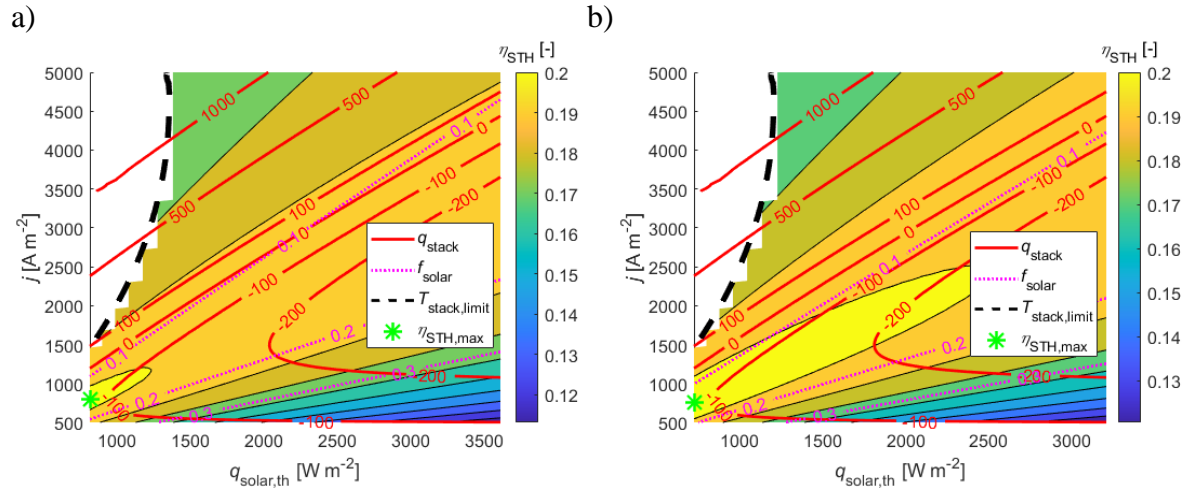
Figure S7. STH efficiency analysis for simulated case with heat recovery effectiveness of 10% and 20%

STH efficiency (contour plot), heat flux of SOE stack (red solid isolines), and solar power input fraction (magenta dotted isolines) as a function of solar thermal input and current density for reference case. Black dashed lines indicate lower (900 K) and upper (1300 K) stack temperature limits. Heat recovery effectiveness a) 10% ($\eta_{HX} = 28.8\%$) and b) 20% ($\eta_{HX} = 59.3\%$). Maximum STH efficiency is for a) 20.15% and b) 20.48% (indicated by green asterisk).

Supplementary Note 5 – Transient characterization of solar cavity-receiver

The transient thermal behavior of the solar cavity-receiver was analyzed experimentally and theoretically by a lumped parameter thermal equivalent resistance network model.

Thermal equivalent resistance network model - The transient response of the solar cavity-receiver in terms of the fluid temperature is described as:[4]

$$\frac{T_{\text{fluid}}(t) - T_{\text{fluid}}(t \to \infty)}{T_{\text{fluid}}(t=0) - T_{\text{fluid}}(t \to \infty)} = e^{-\frac{t}{\tau}}, \tag{S1}$$

where t is the time and τ is the thermal time constant ($\tau = m \cdot c_{\text{p}} / (U \cdot A_{\text{conv}})$). m is the mass of the solar cavity-receiver, c_{p} is the specific heat capacity of Inconel 600, U is the total heat transfer coefficient, and A_{conv} is the inner surface of the solar cavity-receiver tubes. Per definition, for $t = 0$, the thermal solar power input and/or the flow conditions are changed and stay constant for $t > 0$. The experimental determination of the thermal time constant was achieved by exponential regression (least-squares fitting) of the experimental results to eq. S1. An equivalent thermal resistance analysis was applied, considering in-series radiation and convection from the tube surface to the heat transfer fluid as depicted in Figure S8 (control volume in a), and thermal resistance model in b). Conduction was neglected given the small wall thickness (1mm), the large thermal conductivity of Inconel steel (5 W m^{-1} K^{-1}),[5] and heat fluxes in the range of 670 W m^{-2}. The overall heat transfer coefficient is therefore:

$$UA_{\text{conv}} = \frac{1}{\left((h_{\text{rad}} A_{\text{conv}})^{-1} + (h_{\text{conv}} A_{\text{conv}})^{-1} \right)} \tag{S2}$$

h_{conv} is the convective heat transfer coefficient, an average for the anodic and cathodic flows derived from the Nusselt correlation (Nu = 3.66) for laminar flows (Re < 2300) in fully developed flows in circular pipes,[4] assuming fully gaseous flows in the solar cavity-receiver (no two-phase flow). h_{rad} is the radiative heat transfer coefficient approximated by:

$$h_{\text{rad}} = \frac{\varepsilon \cdot \sigma \cdot (T_{\text{solar}}^4 - T_{\text{cav}}^4)}{T_{\text{solar}} - T_{\text{cav}}} \cdot \frac{A_{\text{aper}}}{A_{\text{conv}}} \tag{S3}$$

where $\varepsilon = 1$ is the emissivity of the solar cavity-receiver equal to the apparent absorptivity, σ is the Stefan-Boltzmann constant. Note that the surface ratio ($A_{\text{aper}}/A_{\text{conv}}$) was used to project the radiative heat transfer coefficient (relevant for the aperture of the cavity) onto the convective surface. T_{solar} is then approximated by the equivalent black body temperature:

$$T_{\text{solar}} = \left(\frac{\dot{Q}_{\text{solar,th}}}{\sigma} \right)^{0.25} \tag{S4}$$

where $\dot{Q}_{\text{solar,ap}}$ is the incident solar radiation at the aperture (thermal part of solar power input to reactor).
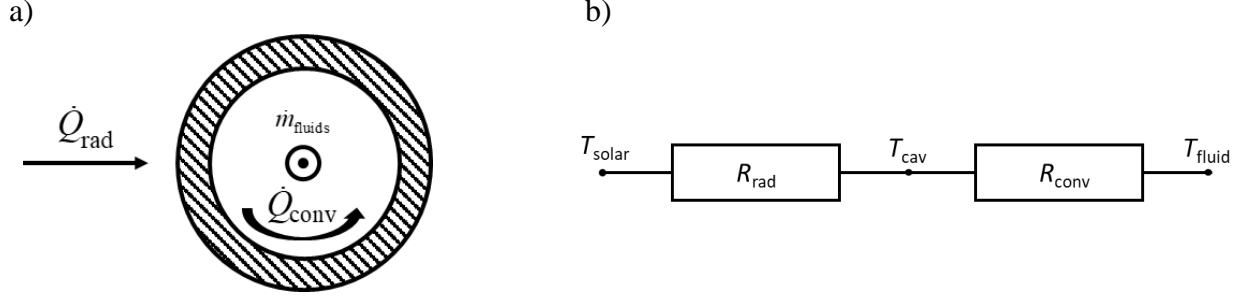
Figure S8. Thermal equivalent resistance network model for solar cavity-receiver
(a) Control volume of the solar cavity-receiver tube (cross-section) for the 1D thermal network circuit analysis. Indicated are the net radiative heat exchange, the convective heat exchange and the mass flow rate of the fluids. (b) 1D thermal network circuit comprising the radiative and convective resistances.

Transient results - The transient behavior of the solar cavity-receiver was tested for SFC-open circuit conditions (campaign 1, type 2). In Figure S9a, two transient example runs are shown indicating measured anodic and cathodic flow temperatures at the outlet as well as the thermal solar power input as a function of the normalized time ($t^* = t / t_{max}$) with $t_{max} = 159$ min for SFC 4/4 and $t_{max} = 267$ min for SFC 8/8. For both cases, $\dot{Q}_{solar,th}$ was increased stepwise up to 2.1 kW.
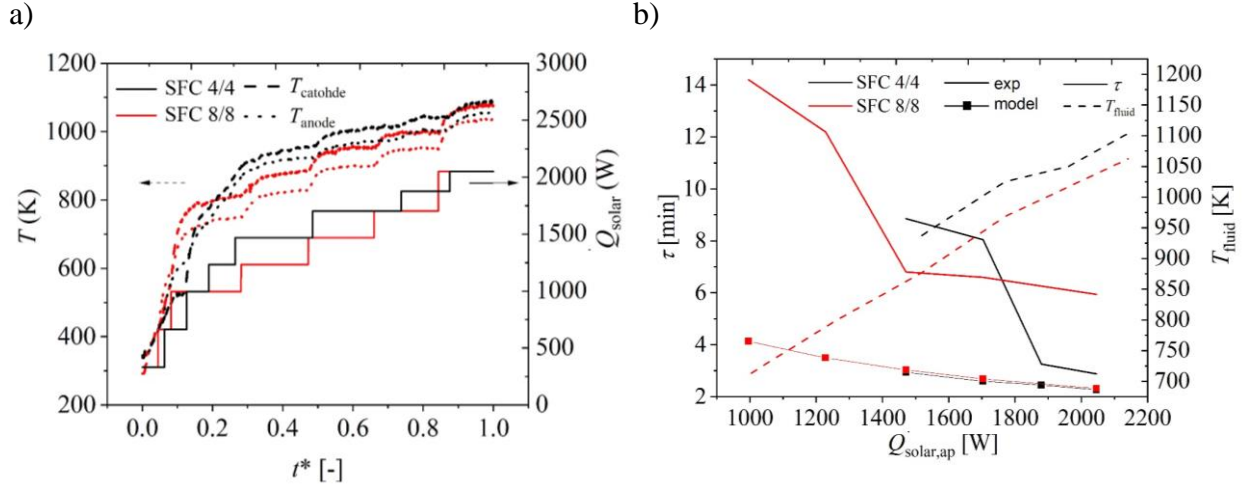
Figure S9. Transient temperature evolution and thermal time constant analysis of solar cavity-receiver
a) Two transient example runs for SFC 4/4 and SFC 8/8. The measured anodic and cathodic flow temperatures at the outlet as well as the solar input at the aperture are plotted as a function of normalized time (total times are 159 min and 267 min for SFC 4/4 and SFC 8/8, respectively). b) Thermal time constant derived from experimental data and 1D thermal resistance circuit model and fluid temperature as a function of solar power input at the aperture for SFCs of 4/4 and 8/8.

The higher SFC leads to lower temperatures at steady state. The maximum outlet temperatures were obtained for the largest $\dot{Q}_{solar,th}$, thus $T_{anode} = 1056$ K and $T_{cathode} = 1087$ K for SFC 4/4, and $T_{anode} = 1036$ K and $T_{cathode} = 1077$ K for SFC 8/8. For both SFCs, the largest temperature difference

between the anode and cathode flow was <100 K, resulting in a temperature gradient of <20 K cm^{-1} in the SOE stack (width of 5 cm), slightly higher than the recommended gradient of 10 K cm^{-1}.[6]

Figure S9b shows the thermal time constant derived from experiments and the thermal equivalent resistance model and measured fluid temperature as a function of $\dot{Q}_{solar,th}$ for SFCs of 4/4 and 8/8. The steady-state consideration started for $\dot{Q}_{solar,th} > 1000$ W ($t^* > 0.13$) and $\dot{Q}_{solar,th} > 1468$ W ($t^* > 0.47$) for SFC 8/8 and SFC 4/4, respectively. Generally, T_{fluid} increased monotonically with increasing $\dot{Q}_{solar,th}$, where SFC 4/4 showed ~5% larger temperatures than SFC 8/8. For both SFCs, the experimental and modeled thermal time constants decrease monotonically with increasing $\dot{Q}_{solar,th}$. The experimentally determined thermal time constant ranged from $\tau = 5.94 – 14.2$ min for SFC 8/8 and $\tau = 2.9 – 8.9$ min for SFC 4/4. The difference between SFC 4/4 and SFC 8/8, and thus mass flow rate variations, showed no correlation with respect to the thermal time constant. The comparison to the results obtained by the thermal equivalent resistance network approach showed a large discrepancy (a factor of 3.5 for SFC 4/4 and $\dot{Q}_{solar,th} = 1.0$ kW). The hypothesis for the main differences is that they originate from model simplifications (worst-case scenario analysis), resulting in an overestimation of the heat transfer, and thus predicting lower time constants. Nevertheless, we observed that the thermal equivalent resistance circuit model was able to predict the order of magnitude of the transient time constants. h_{conv} was $50 – 60$ W m^{-2} K^{-1} and h_{rad} was of similar magnitude ($20 – 30$ W m^{-2} K^{-2}), implying that neither heat transfer mode was dominating. No correlation between SFC 4/4 or SFC 8/8 and $\dot{Q}_{solar,th}$ is observed. The convective transport is invariant with respect to the Reynolds number (mass flow rate), and thus the difference (<3%) in the convective heat transfer coefficient between both SFCs results from the fluid temperature difference only influencing the thermal conductivity of the fluids. For increasing $\dot{Q}_{solar,th}$ (and thus T_{fluid}), the radiative heat transfer coefficient increases with the temperature to the power of 3 (eq. S4), resulting in a decreasing thermal time constant, which is consistent with the observation of the experimental data.

Supplementary Note 6 – Integrated operation of solar reactor

Figure S10 shows the energy breakdown of the integrated solar reactor operated at thermoneutral conditions. The highest STH efficiency was $\eta_{STH} = 3.33\%$ obtained for the highest SFC (SFC 4/4) and largest solar thermal and solar electric input, i.e. $\dot{Q}_{solar,th} = 2.1$ kW and $\dot{Q}_{solar,PV} = 0.4$ kW. The heat losses in the solar cavity-receiver have the largest contribution (74 – 87% from total solar input). The thermal energy balance does not vary for the 6 cases due to the small SOE stack temperature range and the thermoneutral operation of the SOE stack. The second largest contribution are the PV losses, which increase with increasing thermoneutral current density of the SOE stack and have the maximum contribution of 12.6% for the case yielding the highest STH efficiency.

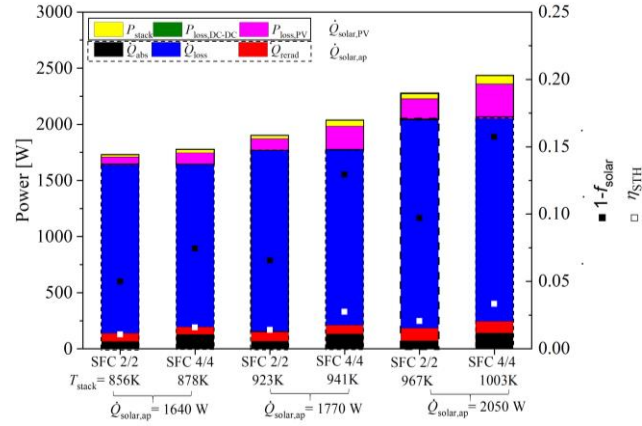**Figure S10. Thermal and electric power input and output of the experimental reactor**

Breakdown of thermal and electric power in- and outputs of the experimental integrated reactor operated at thermoneutral conditions for solar thermal input ranging from 1.6 – 2.0 kW, for solar input for the PV cells ranging from 0.1 – 0.4 kW, and for SFCs 2/2 and 4/4. Right *y*-axis indicates the STH efficiency and the solar factor.

Supplementary Note 7 – Data for water/hydrogen (ΔH, ΔG, ΔS·T)

Table S4. Data for water/hydrogen (ΔH, ΔG, ΔS·T)

Tabulated data for water/hydrogen (ΔH, ΔG, ΔS·T) for a temperature range of 300 – 1555 K.

T [K]	ΔH [kJ mol^{-1}]	ΔG [kJ mol-1]	$\Delta S \cdot T$ [kJ mol-1]	T [K]	ΔH [kJ mol^{-1}]	ΔG [kJ mol-1]	$\Delta S \cdot T$ [kJ mol-1]	T [K]	ΔH [kJ mol^{-1}]	ΔG [kJ mol-1]	$\Delta S \cdot T$ [kJ mol-1]	T [K]	ΔH [kJ mol^{-1}]	ΔG [kJ mol-1]	$\Delta S \cdot T$ [kJ mol-1]
300	241.84473	228.49953	13.3452	625	244.86363	212.76056	32.10307	950	247.40481	195.47387	51.93095	1275	249.26741	177.39894	71.86848
305	241.89522	228.2767	13.61852	630	244.9067	212.50356	32.40314	955	247.43912	195.20045	52.23867	1280	249.29018	177.11705	72.17313
310	241.9455	228.05303	13.89247	635	244.94967	212.24622	32.70344	960	247.47327	194.92686	52.54641	1285	249.31279	176.83508	72.4777
315	241.99559	227.82856	14.16703	640	244.99253	211.98855	33.00398	965	247.50725	194.6531	52.85416	1290	249.33523	176.55303	72.78221
320	242.0455	227.60329	14.44221	645	245.03528	211.73054	33.30474	970	247.54107	194.37915	53.16192	1295	249.35752	176.27088	73.08663
325	242.09523	227.37724	14.71798	650	245.07793	211.4722	33.60573	975	247.57472	194.10504	53.46969	1300	249.37964	175.98865	73.39099
330	242.14478	227.15043	14.99435	655	245.12047	211.21353	33.90694	980	247.60821	193.83075	53.77746	1305	249.4016	175.70634	73.69527
335	242.19418	226.92287	15.27131	660	245.1629	210.95453	34.20837	985	247.64153	193.55629	54.08524	1310	249.42341	175.42394	73.99947
340	242.24342	226.69458	15.54884	665	245.20523	210.69522	34.51001	990	247.67468	193.28166	54.39302	1315	249.44505	175.14145	74.3036
345	242.2925	226.46556	15.82694	670	245.24744	210.43559	34.81186	995	247.70766	193.00686	54.7008	1320	249.46654	174.85889	74.60765
350	242.34144	226.23583	16.10561	675	245.28955	210.17564	35.11391	1000	247.74048	192.7319	55.00857	1325	249.48788	174.57625	74.91163
355	242.39023	226.0054	16.38482	680	245.33154	209.91538	35.41616	1005	247.77312	192.45678	55.31634	1330	249.50906	174.29352	75.21554
360	242.43888	225.77429	16.66459	685	245.37342	209.65482	35.71861	1010	247.80559	192.18149	55.6241	1335	249.53008	174.01072	75.51937
365	242.48739	225.5425	16.94489	690	245.41519	209.39395	36.02125	1015	247.8379	191.90604	55.93185	1340	249.55096	173.72783	75.82312
370	242.53577	225.31005	17.22572	695	245.45685	209.13277	36.32408	1020	247.87003	191.63044	56.23959	1345	249.57168	173.44487	76.1268
375	242.58403	225.07694	17.50708	700	245.49839	208.8713	36.62709	1025	247.90199	191.35468	56.54731	1350	249.59224	173.16183	76.43041
380	242.63215	224.8432	17.78896	705	245.5398	208.60953	36.93028	1030	247.93377	191.07876	56.85501	1355	249.61266	172.87872	76.73394
385	242.68016	224.60882	18.07134	710	245.58111	208.34746	37.23364	1035	247.96538	190.80269	57.16269	1360	249.63293	172.59553	77.03739
390	242.72804	224.37381	18.35423	715	245.62229	208.08511	37.53718	1040	247.99682	190.52646	57.47036	1365	249.65304	172.31227	77.34078
395	242.77581	224.1382	18.63761	720	245.66335	207.82247	37.84088	1045	248.02808	190.25009	57.77799	1370	249.67301	172.02893	77.64408
400	242.82346	223.90198	18.92148	725	245.70429	207.55954	38.14475	1050	248.05917	189.97356	58.0856	1375	249.69284	171.74552	77.94731
405	242.871	223.66517	19.20583	730	245.74511	207.29634	38.44878	1055	248.09008	189.69689	58.39318	1380	249.71251	171.46204	78.25047
410	242.91842	223.42776	19.49066	735	245.78581	207.03285	38.75296	1060	248.12081	189.42007	58.70074	1385	249.73204	171.17849	78.55355
415	242.96574	223.18979	19.77595	740	245.82639	206.76909	39.0573	1065	248.15137	189.14311	59.00825	1390	249.75142	170.89487	78.85655
420	243.01295	222.95124	20.06171	745	245.86683	206.50505	39.36178	1070	248.18174	188.86601	59.31574	1395	249.77066	170.61118	79.15948
425	243.06005	222.71213	20.34792	750	245.90715	206.24074	39.66641	1075	248.21194	188.58876	59.62318	1400	249.78976	170.32742	79.46234
430	243.10705	222.47247	20.63458	755	245.94735	205.97616	39.97118	1080	248.24196	188.31137	59.93059	1405	249.80871	170.04359	79.76512
435	243.15394	222.23226	20.92168	760	245.98741	205.71132	40.27609	1085	248.2718	188.03385	60.23795	1410	249.82752	169.7597	80.06783
440	243.20073	221.99151	21.20922	765	246.02735	205.44622	40.58113	1090	248.30146	187.75618	60.54527	1415	249.84619	169.47573	80.37046
445	243.24742	221.75023	21.49719	770	246.06715	205.18085	40.8863	1095	248.33094	187.47839	60.85255	1420	249.86472	169.19171	80.67301
450	243.29401	221.50843	21.78558	775	246.10682	204.91523	41.1916	1100	248.36023	187.20045	61.15978	1425	249.88311	168.90762	80.9755
455	243.34049	221.26611	22.07438	780	246.14636	204.64935	41.49701	1105	248.38933	186.92239	61.46694	1430	249.90136	168.62346	81.2779
460	243.38688	221.02328	22.3636	785	246.18577	204.38321	41.80255	1110	248.41824	186.64419	61.77404	1435	249.91947	168.33924	81.58023
465	243.43318	220.77995	22.65323	790	246.22504	204.11683	42.1082	1115	248.44694	186.36587	62.08107	1440	249.93745	168.05496	81.88249
470	243.47937	220.53612	22.94325	795	246.26417	203.8502	42.41397	1120	248.47545	186.08741	62.38804	1445	249.95528	167.77061	82.18467
475	243.52547	220.2918	23.23367	800	246.30316	203.58332	42.71984	1125	248.50376	185.80883	62.69493	1450	249.97299	167.4862	82.48678
480	243.57147	220.04699	23.52448	805	246.34202	203.3162	43.02582	1130	248.53187	185.53012	63.00175	1455	249.99055	167.20174	82.78881
485	243.61737	219.8017	23.81567	810	246.38074	203.04884	43.3319	1135	248.5598	185.25129	63.3085	1460	250.00798	166.91721	83.09077
490	243.66318	219.55595	24.10723	815	246.41932	202.78124	43.63808	1140	248.58753	184.97234	63.61518	1465	250.02528	166.63262	83.39266
495	243.70889	219.30972	24.39917	820	246.45776	202.51341	43.94435	1145	248.61506	184.69327	63.9218	1470	250.04244	166.34798	83.69447
500	243.75451	219.06304	24.69148	825	246.49605	202.24534	44.25072	1150	248.64241	184.41407	64.22834	1475	250.05947	166.06327	83.9962
505	243.80003	218.81589	24.98414	830	246.53421	201.97703	44.55717	1155	248.66957	184.13476	64.53481	1480	250.07637	165.77851	84.29786
510	243.84546	218.5683	25.27716	835	246.57222	201.7085	44.86371	1160	248.69654	183.85533	64.84121	1485	250.09314	165.49369	84.59945
515	243.89079	218.32027	25.57053	840	246.61008	201.43975	45.17033	1165	248.72332	183.57578	65.14754	1490	250.10977	165.20882	84.90096
520	243.93603	218.07179	25.86424	845	246.6478	201.17076	45.47704	1170	248.74992	183.29612	65.45379	1495	250.12628	164.92389	85.20239
525	243.98117	217.82288	26.15829	850	246.68537	200.90156	45.78382	1175	248.77633	183.01635	65.75998	1500	250.14266	164.6389	85.50376
530	244.02622	217.57354	26.45268	855	246.7228	200.63213	46.09067	1180	248.80256	182.73647	66.06609	1505	250.15891	164.35386	85.80505
535	244.07117	217.32377	26.7474	860	246.76007	200.36248	46.39759	1185	248.8286	182.45647	66.37213	1510	250.17503	164.06877	86.10626
540	244.11602	217.07359	27.04244	865	246.7972	200.09262	46.70458	1190	248.85447	182.17636	66.6781	1515	250.19102	163.78362	86.4074
545	244.16078	216.82299	27.3378	870	246.83418	199.82255	47.01163	1195	248.88015	181.89615	66.984	1520	250.20689	163.49842	86.70847
550	244.20545	216.57198	27.63347	875	246.87101	199.55226	47.31875	1200	248.90565	181.61583	67.28982	1525	250.22263	163.21317	87.00946
555	244.25002	216.32056	27.92945	880	246.90769	199.28176	47.62592	1205	248.93098	181.3354	67.59558	1530	250.23825	162.92787	87.31038
560	244.29449	216.06875	28.22574	885	246.94421	199.01106	47.93315	1210	248.95614	181.05487	67.90127	1535	250.25374	162.64252	87.61123
565	244.33886	215.81653	28.52233	890	246.98058	198.74015	48.24043	1215	248.98111	180.77423	68.20688	1540	250.26911	162.35711	87.912
570	244.38314	215.56393	28.81921	895	247.0168	198.46903	48.54777	1220	249.00591	180.4935	68.51242	1545	250.28436	162.07166	88.2127
575	244.42732	215.31093	29.11638	900	247.05286	198.19771	48.85515	1225	249.03054	180.21266	68.81788	1550	250.29948	161.78616	88.51332
580	244.4714	215.05756	29.41384	905	247.08877	197.9262	49.16257	1230	249.05499	179.93172	69.12328	1555	250.31448	161.50061	88.81387
585	244.51538	214.8038	29.71158	910	247.12452	197.65448	49.47004	1235	249.07927	179.65068	69.42859				
590	244.55926	214.54967	30.0096	915	247.16011	197.38257	49.77754	1240	249.10338	179.36954	69.73384				
595	244.60305	214.29516	30.30788	920	247.19555	197.11047	50.08508	1245	249.12732	179.08831	70.03901				
600	244.64673	214.04029	30.60644	925	247.23083	196.83817	50.39266	1250	249.15109	178.80698	70.34411				
605	244.69032	213.78506	30.90526	930	247.26594	196.56568	50.70026	1255	249.17469	178.52556	70.64913				
610	244.7338	213.52946	31.20433	935	247.3009	196.293	51.0079	1260	249.19812	178.24404	70.95408				
615	244.77718	213.27351	31.50366	940	247.3357	196.02014	51.31556	1265	249.22138	177.96243	71.25895				
620	244.82045	213.01721	31.80324	945	247.37034	195.7471	51.62324	1270	249.24448	177.68073	71.56375				

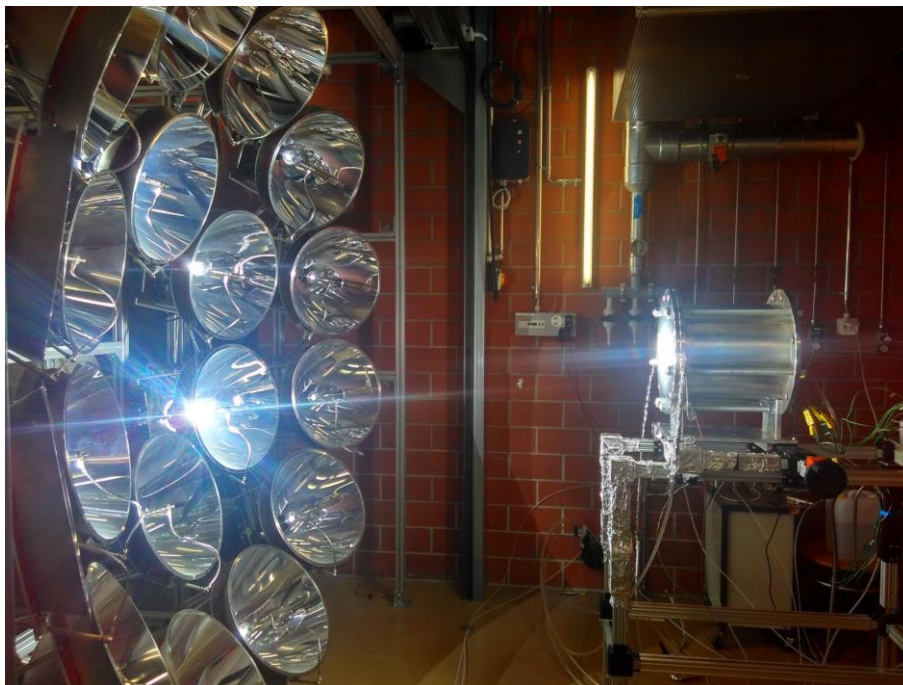**Supplementary Note 8 – Photos of experimental setup**

Figure S11. Photo of integrated reactor in LRESE's high-flux solar simulator
Photo of the integrated reactor (right) in operation in LRESE's high-flux solar simulator (left).
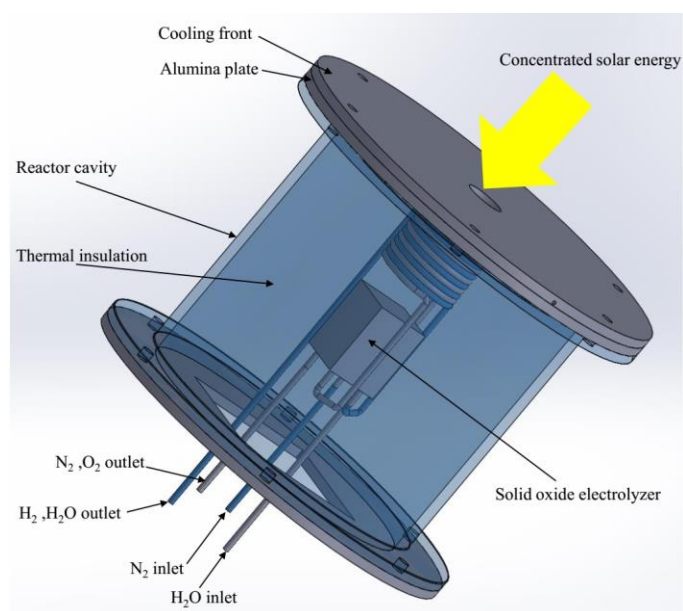

Figure S12. CAD drawing of integrated reactor
CAD drawing of the integrated reactor with arrow indicating direction of concentrated light.
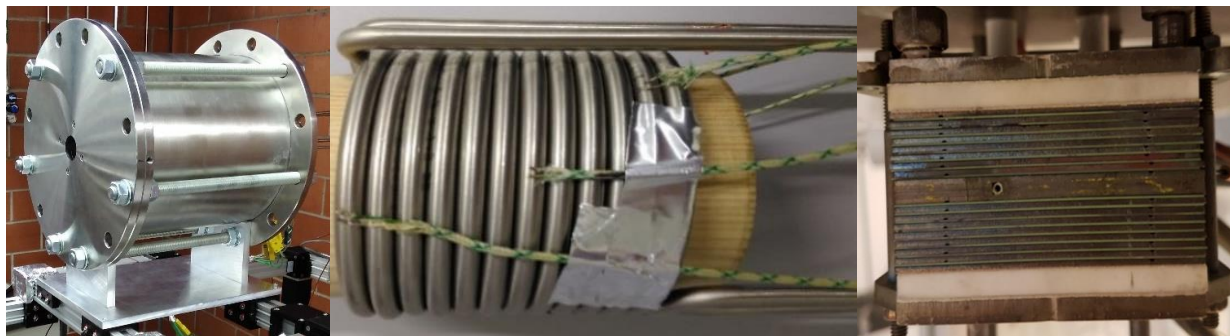
Figure S13. Photos of integrated reactor and its components
Close up photos of a) stainless steel solar reactor with aperture (aperture diameter 5 cm, water cooled front plate diameter 39.5 cm), b) double helical tube (rolled up on wooden cylinder, helical turning radius is 40 mm) with thermocouples, and c) 16 cells Ni/YSZ/LSM electrolyzer stack (6 x 8 cm^2).

References

1. Stine, W.B., and Diver, R.B. (1994). A compendium of solar dish/Stirling technology.
2. Best Solar Panel Angle: How Do You Find It — And Does it Matter? https://www.solarreviews.com/blog/best-solar-panel-angle.
3. Haussener, S., Hu, S., Xiang, C., Weber, A.Z., and Lewis, N.S. (2013). Simulations of the irradiation and temperature dependence of the efficiency of tandem photoelectrochemical water-splitting systems. Energy Environ. Sci. *6*, 3605–3618.
4. Incropera, F.P., Dewitt, D.P., Bergman, T.L., and Lavine, A.S. (2007). Fundamentals of Heat and Mass Transfer 6th ed. (John Wiley & Sons, Ltd).
5. Hosaeus, H., Seifter, A., Kaschnitz, E., and Pottlacher, G. (2001). Thermophysical properties of solid and liquid Inconel 718 alloy. High Temp. Press. *33*, 405–410.
6. Aguiar, P., Adjiman, C.S., and Brandon, N.P. (2004). Anode-supported intermediate temperature direct internal reforming solid oxide fuel cell. I : model-based steady-state performance. J. Power Sources *138*, 120–136.